Revision 1: Pressure-induced Pbca-P2_1/c phase transition of natural orthoenstatite: Compositional effect and its geophysical implications

Jin S. Zhang[1,*], Bruno Reynard[2], Gilles Montagnac[2], Ru Cheng Wang[3] and Jay D. Bass[1]

[1] Department of Geology, University of Illinois, Urbana, Illinois 61801, U.S.A.

[2]Laboratoire de Géologie de Lyon, CNRS, Ecole Normale Supérieure de Lyon, France

[3]State Key Laboratory for Mineral Deposits Research, Department of Earth Sciences, Nanjing University, Nanjing 210093, China

[*]Email: zhang72@illinois.edu

Abstract

Raman spectroscopy has been employed to investigate possible compositional effects on the high-pressure phase transition of Mg-rich orthoenstatite to a newly-discovered P2_1/c phase. Three natural orthoenstatite samples were used in this study: near end-member Mg orthoenstatite (Zabargad Island, Egypt), Al-free Fe-bearing orthoenstatite (Morogoro, Tanzania), and Al-rich Fe,Ca-bearing orthoenstatite (Kilbourne Hole, New Mexico). Experiments were carried out at room temperature. For all samples, the high-pressure phase transition is characterized by a splitting of the 660-680 cm^{-1} doublet in the Raman spectrum into a triplet, with a corresponding change of peak intensities. These spectral changes are caused by the lowered symmetry of the high-pressure phase, as indicated by structural refinement from single-crystal X-ray diffraction results. The high-pressure phase of all samples appears to have space group P2_1/c. No evidence for a C2/c phase was observed. Our results indicate that upon compression, 10mol% Fe decreases the onset pressure of formation of the high-pressure P2_1/c phase by about 1 GPa. Results for the Kilbourne Hole OEN show that a combined enrichment of Al and Ca contents increases the onset pressure of formation of HPCEN2 (upon compression) by over 3 GPa relative to Tanzania OEN. Upon

24 decompression, all samples revert to single-crystals of the orthoenstatite starting phase. Our
25 measurements suggest that orthoenstatite is the prevalent phase of Mg-rich pyroxene throughout the
26 uppermost mantle, whereas the newly discovered $P2_1/c$ phase might be present near the bottom of
27 uppermost mantle, slightly shallower than the top of the transition zone.

28 Keywords: orthoenstatite, high-pressure clinoenstatite, high-pressure phase transition, upper mantle,
29 Raman spectroscopy

Introduction

Mg-rich Fe-bearing pyroxene with approximate composition $(Mg,Fe)SiO_3$, is one of the major minerals in Earth's uppermost mantle. Four polymorphs of $(Mg,Fe)SiO_3$ are potentially stable under upper mantle conditions: orthoenstatite (OEN) with space group Pbca (Morimoto and Koto 1969), low-pressure clinoenstatite (LPCEN) with space group $P2_1/c$ (Morimoto et al. 1960), high-pressure clinoenstatite (HPCEN) with space group C2/c (Angel et al. 1992), and a newly discovered high pressure monoclinic polymorph (HPCEN2) also with space group $P2_1/c$ (Zhang et al. 2012). Although the equilibrium stability fields for these four polymorphs have not yet been firmly established, the discovery of the new $P2_1/c$ structure has potentially important implications for the phase relations in the $(Mg,Fe)SiO_3$ system and for upper mantle mineralogy.

Experimentally determined pressures for the transition from OEN to the high-pressure polymorph HPCEN2 span a wide range for different experiments using different samples with different techniques. For example, Raman spectroscopy on synthetic flux-grown $MgSiO_3$ (containing minor amounts of Li, Mo, V), compressed in a diamond anvil cell (DAC), indicate a transition pressure of between 6.1GPa and 12.0GPa in an argon pressure-transmitting medium (Chopelas 1999), and between 9.5GPa and 10GPa in water (Lin 2003). Multi-anvil ultrasonic experiments constrained the transition pressure to be between 9.6 and 11.8GPa (Kung et al. 2004). For natural orthoenstatite from San Carlos, containing 8mol%Fe and 2.5wt%Al, the transition does not occur until 14.26 GPa in a neon pressure medium, as determined from single-crystal X-ray diffraction experiments (Zhang et al. 2012). For orthoenstatite from Kilbourne Hole, containing 9mol%Fe 5wt%Al, there is no evidence for this phase transition up to 12.5 GPa by stimulated light scattering in a DAC (Chai et al., 1997). These discrepancies on the transition pressure suggest that chemical composition (both natural cation substitutions such Al, Fe, Ca, as well as the incorporation of

artificial flux components such as Li, Mo, V), as well as the pressure medium used, could both have a significant effect on the transition pressure and possibly the phase relations between OEN, HPCEN LPCEN and HPCEN2. Thus, it is important to separate the effects of chemistry from effects of the pressure medium in order to investigate the effect of composition on the stability of the $P2_1/c$ phase. Moreover, orthoenstatite in Earth's mantle does not exist as $MgSiO_3$, but will almost certainly contain Fe, Al, and Ca as minor elements, with the exact composition dependent on depth. In general, the Fe content of OEN tends to be relatively constant with increasing depth, whereas Ca and Al content will likely decrease as enstatite is progressively dissolved into Ca-rich clinopyroxene and garnet (Akaogi and Akimoto 1977; Irifune and Ringwood 1987; Brey et al. 2008). Thus it is important to evaluate the phase transition pressures of OEN for a variety of potential mantle compositions. We thus chose to study two natural Fe-bearing samples representative of possible upper mantle compositions, and a composition near the MgSiO3 end-member for the sake of comparison with prior work and calibration.

In this paper we report the results of in-situ high-pressure room-temperature Raman experiments with several chemically distinct samples loaded together in a sample chamber of a diamond-anvil cell (DAC) to clarify the effects of compositional variations in natural orthoenstatite on the newly discovered Pbca→$P2_1/c$ phase transition.

Sample Description and Experimental Methods

Natural orthenstatite samples from three different locations and with different chemical compositions were used in this study: 1) near end-member $MgSiO_3$ orthoenstatite from Zabargad Island, Egypt; 2) Al-free Fe-bearing orthoenstatite from the Morogoro Region, Tanzania; 3) Al-rich Fe,Ca-

bearing orthoenstatite from Kilbourne Hole, New Mexico. Samples of high optical quality were polished into plate-like samples of ~20 μm thickness using Al_2O_3 abrasive film (down to 0.3 μm grain size). All samples were scratch-free under optical examination, and were cut into pieces approximately 20 – 60 μm wide for compositional analysis and DAC loading.

The chemical composition of each sample was analyzed using a JXA 8100 electron microprobe at Nanjing University. All elemental analyses were performed using an accelerating potential of 15 kV, a beam current of 20 nA, and a beam 1 μm in diameter. Element peaks and backgrounds were measured with counting times of 20 and 10 s, respectively. A ZAF routine correction was used in the data reduction. Hornblende was used as the standard for all the measured elements, yielding results as follows: Zabargad Island (Zabg) $(Mg_{0.994}Fe_{0.002}Al_{0.004})_2(Si_{0.996}Al_{0.004})_2O_6$, or $En_{99}Fs_0Di_0MgTs_1$; Tanzania (Tan) $(Mg_{0.897}Fe_{0.097}Ca_{0.004}Al_{0.002})_2(Si_{0.996}Al_{0.002})_2O_6$, or $En_{89}Fs_{10}Di_1MgTs_0$; and Kilbourne Hole (KBH) $(Mg_{0.835}Fe_{0.090}Ca_{0.020}Al_{0.055})_2(Si_{0.945}Al_{0.055})_2O_6$, or $En_{76}Fs_9Di_4MgTs_{11}$, where En indicates the $Mg_2Si_2O_6$ component, Fs is $Fe_2Si_2O_6$, Di is $CaMgSi_2O_6$, and MgTs is $(MgAl)(SiAl)O_6$.

High-pressure experiments were performed with a membrane-type diamond anvil cell for precise pressure control. Rhenium metal gaskets with an initial thickness of 250 μm were pre-indented to 0.070 mm using 500 μm culet, ultra-low fluorescence diamond anvils. A 250 μm diameter hole in the gasket formed the sample chamber. Three different plate-like samples (maximum ~60 μm width) and several ruby balls were loaded together in the diamond-anvil cell sample chamber (Figure 1). An alcohol mixture (methanol:ethanol=4:1) was loaded as a pressure-transmitting medium. A heat gun was used to warm the chamber (up to 60°C) to help relax differential stresses when needed. Pressure was determined from ruby fluorescence (Mao et al. 1986) before and after the Raman experiment at each pressure; the maximum

pressure difference from the two readings was 0.14 GPa or less. Maximum stress differentials were obtained during decompression runs.

In-situ high-pressure single-crystal Raman spectroscopy experiments were carried out at Ecole Normale Supérieure de Lyon. Raman spectra were obtained using a multichannel Raman microprobe (LabRam HR800 from DILOR) equipped with a confocal microscope configuration that enhances the signal-to-noise ratio by eliminating most of the parasitic light from sample and diamond fluorescence. Experiments were conducted in a backscattering geometry with a Mitutoyo objective that focused the incident laser spot to less than 2 μm in diameter. The scattered Raman light is focused through a 100-micron slit into a spectrograph equipped with a 1800 gr/mm grating and analyzed by a CCD detector, giving a resolution of approximately 2.5 cm^{-1} (Auzende et al. 2004). The accumulation times for Raman spectra were typically 60-120s over the spectral region from 100 cm^{-1} to 1250 cm^{-1}. Peak positions were determined to within 2 cm^{-1} or better depending on sample quality. The 514.5 line of an argon ion laser was used as an excitation source at an output power ranging from 500 to 1500 mW. Only 5 to 10% of this power reaches the sample, due to absorption or reflection from the optical elements and diamonds in the optical path.

Results

High pressure Raman data were collected at 47 different pressures between 0.30(1) GPa and 18.01(2) GPa in several compression and decompression cycles The number of Raman-active modes in orthoenstatite is predicted to be 120 (Ferraro 1975). However, the number of observed Raman bands is smaller in any given run due to the weak intensity and/or overlap of many bands, and the strong orientation dependence of intensity. Because the edge filter used to cut off Rayleigh scattering limits the

116 measured Raman shifts to above100 cm^{-1}, we were not able to observe the lowest frequency bands of
117 OEN. Another limitation included the overlap of the strong methanol ethanol C-O stretching band at
118 ~1030 cm^{-1} with OEN and HPCEN2 peaks near that frequency shift.

119 We consistently observed 34 bands in Zabg OEN, 40 bands in Zabg HPCEN2; 28 bands in Tan
120 OEN, 26 bands in Tan HPCEN2; 23 bands in KBH OEN, 24 bands in KBH HPCEN2. The results are
121 listed in Tables 1 and 2. Our observations are in good agreement with previous results (Lin 2003,
122 Chopelas 1999; Huang et al. 2000; Stalder et al. 2009; Reynard et al. 2008; Zucker and Shim 2009).
123 Small discrepancies were due to crystal orientation effects, overlap of peaks, and weak intensities of some
124 peaks.

125 Typical Raman spectra of OEN and HPCEN2 for all three samples are shown in Figure 2a. In the
126 low frequency range, the transition is characterized by the occurrence of HPCEN2 peaks (e.g. for Zabg
127 OEN at 12.5GPa, 199.5cm^{-1} , 228.3 cm^{-1}, 341.9 cm^{-1}), with fading OEN peaks (206.6cm^{-1}, 238.5cm^{-1},
128 210.5cm^{-1}, 218.1cm^{-1}, 308.2cm^{-1}, 312.7cm^{-1}). The single most significant characteristic of this
129 transition is splitting of the strong 660-680 cm^{-1} doublet into a triplet (Figure 3), accompanied by a change
130 in the relative intensities of the peaks. The 660-680 cm^{-1} doublet is assigned to the Si-O-Si bending mode
131 of the tetrahedral chains. A change in the number of peaks in that region indicates a change in the number
132 of symmetrically distinct tetrahedral chains, which is diagnostic of the phase transition (Chopelas and
133 Boehler 1992; Ross and Reynard, 1999). The observation of an increase from two to three peaks is
134 consistent with X-ray structural refinements of the HPCEN2 phase, which indicate that the number of
135 distinct tetrahedral (T) chains doubles across the OEN-HPCEN2 transition (Figure 4). In detail, the A site
136 T-chain in the OEN structure splits into two T-chains with the O3-O3-O3 angle changing from
137 160.71(16)° to 148.44(79)° and 216.61(77)°. The B site T-chain in OEN undergoes a change in O3-O3-

O3 angle from 135.44(15)° to 131.94(72)° and 133.13(49)° (Zhang et al. 2012). The large change of angle in the A chain is related to the split of the Raman doublet, whereas the change for the B chain is so small that the associated Raman peak splitting cannot be resolved, thus yielding a spectral triplet instead of a quadruplet. For similar reasons, the doublet of OEN transforms to a single peak in the same frequency region upon transition to HPCEN with space group C2/c (Chopelas and Boehler 1992; Ross and Reynard, 1999). These clear spectral differences makes Raman spectroscopy an efficient tool to differentiate OEN polymorphs from each other (Lin 2004).

Discussion and conclusion

For all three OEN samples, peak splitting associated with the Pbca→$P2_1/c$ phase transition was observed. Evidence for a C2/c phase, which was claimed to be the stable high-pressure phase above ~7-9 GPa (Angel et al. 1992), was not observed over the pressure range of the present experiments. We were able to observe the formation of domains as the transition proceeded (e.g. Figure 2b and c). There are two distinctive characteristics of these domains. Firstly, they developed upon initiation of the transition, and disappeared after the transition was completed (e.g. Figure 2b). All samples were single crystals by optical examination before initiation and after completion of the high-pressure transition. Secondly, the formation of $P2_1/c$ phase domains started from edges of the sample and progressed toward the center (e.g. Zabg OEN Figure 2c). Edges may have a high density of crystal defects that act as nucleation sites for the new phase.

The onset pressure of the Pbca→$P2_1/c$ transition (P_{Tr}) is different for the three samples. For near Mg-end member Zabg OEN, P_{Tr} is between 13.13(11) - 13.41(8) GPa on compression, and between

11.03(1) - 11.13(11) GPa on decompression. For near-Al-free Fe-bearing Tan OEN, P_{Tr} was constrained between 12.38(3) - 12.42(4) and 11.03(1) - 11.13(11) GPa in compression and decompression cycles, respectively. For Al-rich Ca, Fe-bearing KBH OEN, P_{Tr} was constrained as between 15.73(12) - 16.25(14) and 12.18(1) - 12.58(1) GPa during compression and decompression, respectively. A comparison between Zabg OEN and Tan OEn indicates that 10mol% Fe content decreased the onset pressure of the initial formation of HPCEN2 by ~1GPa; however, the comparison between KBH and Tan OEN is more complex, including differences in both Al and Ca contents. KBH OEN contains 0.22 Al per formula unit (pfu, based on 6 oxygens), which is 27.5 times more than in Tan OEN. The Ca content of KBH OEN is 0.040 pfu, which is 5 times more than in Tan OEN. Considering the fact that the Fe contents are very close to each other, the presence of 0.212 pfu more Al and 0.032 pfu more Ca increased the onset pressure of the initial formation of HPCEN2 by over 3 GPa. Notably, it seems that the transition pressure during decompression is less sensitive to composition – ~10mol% Fe does not change decompressional transition pressure while 0.212 pfu more Al and 0.032 pfu more Ca increased it only by about 1 GPa.

Increased repulsion between the M2 site cation and A-site Si was believed to be a key factor in determining the topology of pyroxene structures at higher pressure. Fe prefers M2 sites over the M1 sites as suggested from the structure refinement for both OEN and HPCEN2 (e.g., Zhang et al. 2012). The substitution of Fe atoms into the structure results in a larger M2 site, thus giving the Si-O tetrahedral chains more spatial flexibility, and making this Pbca→$P2_1/c$ transition, which is characterized by tetrahedral rotation, easier to occur at lower pressure. Similar qualitative arguments for the effects of Ca and Al are less obvious, because the effects of these two elements cannot be decoupled in this experiment. We do not rule out the possibility that a small amount of Ca might have a significant effect on the transition pressure, as it has a resolvable effect on the OEN structure (Tribaudino and Nestola 2003).

Additional experiments would be needed to determine pure Ca or Al effects using synthetic samples. However, the much greater abundance of Al over Ca in KBH OEN suggests to us that the enrichment of Al is the primary cause of the increase in the onset of P_{Tr}. The case of Al substitution into the crystal structure is complicated since it involves a coupled substitution mechanism, with half the Al atoms occupying the tetrahedral A site substituting for Si, and half occupying the M1 sites substituting for Mg, resulting in a Mg-Tschermaks component in the KBH OEN. In this case, two competing processes, due to Al occupying two polyhedral sites, will be operative. Although the individual effects of these two substitutions are not resolved by the present experiments, net effect is to increase the phase transition pressure.

In the upper mantle, the Fe content in OEN does not change much with depth, whereas Ca and Al contents decrease with increasing depth (Akaogi and Akimoto 1977; Irifune and Ringwood 1987; Brey et al. 2008). Al and Ca will be enriched in Ca-rich clinopyroxene and garnet in comparison to OEN. Thus, in the 300-450km depth range where this phase transition might occur, the composition of OEN is probably between San Carlos OEN (Zhang et al. 2012) and Tan OEN, but likely closer to Tan OEN. Neglecting thermal effects, our results suggest a transition depth of about 350-400km (if the OEN has not yet completely dissolved into the garnet structure), just above the 410km discontinuity. Additional studies, including high temperature measurements of the stability of HPCEN2, and single-crystal elasticity measurements, will be required to obtain better estimates of the depth at which the OEN-HPCEN2 transition occurs in the mantle, and its seismic signature.

Acknowledgments

This work was supported by the National Science Foundation (NSF) under Grant EAR07-38871, the Consortium for Materials Properties Research in Earth Sciences (COMPRES) under NSF Cooperative Agreement EAR 11-57758, and an international cooperative program between University of Illinois at Urbana-Champaign and Centre National de la Recherche Scientifique (CNRS), France. The Raman facility in Lyon is supported by Institut National des Sciences de l'Univers. We thank Hervé Cardon for help with our experiments. We are grateful to George Rossman (Caltech) and George Harlow (Am. Museum of Natural History) for providing samples.

213 References

214 Angel, R.J., Chopelas, A., and Ross, N.L. (1992) Stability of high-density clinoenstatite at upper-mantle
215 pressures. Nature, 358, 322-324.

216 Akaogi, M. and Akimoto, S. (1977) Pyroxene-garnet solid-solution equilibria in the systems $Mg_4Si_4O_{12}$-
217 $Mg_3Al_2Si_3O_{12}$ and $Fe_4Si_4O_{12}$-$Fe_3Al_2Si_3O_{12}$ at high pressures and temperatures, Physics of the Earth
218 and Planetary Interiors, 15, 90-106.

219 Auzende, A.-L., Daniel, I., Reynard, B., Lemaire, C., and Guyot, F. (2004) High-pressure behaviour of
220 serpentine minerals: a Raman spectroscopic study. Physics and Chemistry of Minerals, 31, 269-
221 277.

222 Brey, G. P., Bulatov, V. K. and Girnis, A.V. (2008) Geobarometry for Peridotites: Experiments in Simple
223 and Natural Systems from 6 to 10 GPa. Journal of Petrology, 49, 3-24.

224 Chai, M., Brown, J. M., and Slutsky, L. J. (1997) The elastic constants of an aluminous orthopyroxene to
225 12.5 GPa, Journal of Geophysical Research, 102(B7), 14779–14785.

226 Chopelas, A. (1999) Estimates of mantle relevant Clapeyron slopes in the $MgSiO_3$ system from high-
227 pressure spectroscopic data. American Mineralogist, 84, 233-244.

228 Chopelas, A. and Boehler, R. (1992) Raman spectroscopy of high pressure $MgSiO_3$ phases synthesized in
229 a CO2 laser heated diamond anvil cell: Perovskite and clinopyroxene. In Y. Syono, and M.H.
230 Manghnani, Eds, High-Pressure Research: Application to Earth and Planetary Sciences,
231 Geophysical Monograph, 67, p. 101–108. American Geophysical Union, Washington, D.C.

Ferraro, J.R. (1975) Factor Group Analysis for Some Common Minerals. Applied Spectroscopy, 29, 418-421.

E. Huang, Chen, C.H., Huang, T., Lin, E.H. and Xu, Ji-an. (2000) Raman spectroscopic characteristics of Mg-Fe-Ca pyroxenes. American Mineralogist, 85, 473–479.

Irifune, T. and Ringwood, A.E. (1987) Phase Transformations in Primitive MORB and pyrolite compisitions to 25 GPa and some geophysical implications. In M.H. Manghnani and Y. Syono, Eds., High-Pressure Research in Mineral Physics, 39, p. 231-242. Geophysical Monograph, American Geophysical Union, Washington DC.

Kung, J., Li, B., Uchida, T., Wang, Y., Neuville, D., and Liebermann, R. C. (2004) In situ measurements of sound velocities and densities across the orthopyroxene → high-pressure clinopyroxene transition in $MgSiO_3$ at high pressure, Physics of Earth and Planetary Interiors, 147, 27-44.

Lin, C.-C. (2003), Pressure-induced metastable phase transition in orthoenstatite ($MgSiO_3$) at room temperature: a Raman spectroscopic study. Journal of Solid State Chemistry, 174, 403-411.

Lin, C.-C. (2004), Pressure-induced polymorphism in enstatite ($MgSiO_3$) at room temperature: clinoenstatite and orthoenstatite. Journal of Physics and Chemistry of Solids, 65, 913-921.

Mao, H.K., Xu, J., and Bell, P.M. (1986) Calibration of the ruby pressure gauge to 800 kbar under quasi-hydrostatic conditions. Journal of Geophysical Research, 91, 4673-4676.

Morimoto, N., Appleman, D.E., and Evans, H.T. Jr. (1960) The crystal structures of clinoenstatite and pigeonite. Zeitschrift für Kristallographie, 114, 120-147.

Morimoto, N. and Koto, K. (1969) The crystal structure of orthoenstatite. Zeitschrift für Kristallographie, 129, 65-83.

Nestola, F. and Tribaudino, M. (2003) The structure of Pbca orthopyroxenes along the join diopside-enstatite ($CaMgSi_2O_6$-$Mg_2Si_2O_6$). European Journal of Mineralogy, 15, 365-371.

Reynard, B., Bass, J. D. and Jackson, J. M. (2008) Rapid identification of steatite–enstatite polymorphs at various temperatures. Journal of the European Ceramic Society, 28, 2459–2462.

Ross, N.L. and Reynard, B. (1999) The effects of iron on the $P2_1/c$ to C2/c transitions in $(Mg,Fe)SiO_3$ clinopyroxenes. European Journal of Mineralogy, 11, 585–589.

Stalder, R., Kronz, A. and Schmidt, B. C. (2009) Raman spectroscopy of synthetic $(Mg,Fe)SiO_3$ single crystals. An analytical tool for natural orthopyroxenes. European Journal of Mineralogy, 21, 27–32.

Ulmer, P. and Stadler, R. (2001) The $Mg(Fe)SiO_3$ orthoenstatite-clinoenstatite transitions at high pressures and temperatures determined by Raman-spectroscopy on quenched samples. American Mineralogist, 86, 1267-1274.

Zhang, J. S., Dera, P., and Bass, J. D. (2012) A new high-pressure phase transition in natural Fe-bearing orthoenstatite. American Mineraogist, 97, 1070–1074.

Zucker, R. and Shim, S.-H. (2009) In situ Raman spectroscopy of $MgSiO_3$ enstatite up to 1550 K. American Mineralogist, 94, 1638–1646.

271 Figure Captions

272 Figure 1 – Diamond anvil cell sample chamber

273 Figure 2 –

274 a. Selected Raman spectra of OEN and HPCEN2 for all three samples at high pressures. The 660-680

275 cm^{-1} doublet-to-triplet changes for each of the samples are indicated with red arrows.

276 b. Optical observation of the OEN→HPCEN2 phase transition in the mixed phase region for sample Tan.

277 c. Optical observation of the OEN→HPCEN2 phase transition in the mixed phase region for sample Zabg.

278 Figure 3 – Raman frequency shifts of the 660-680 cm^{-1} doublet/triplet as a function of pressure

279 a. Zabargad Island, Egypt

280 b. Morogoro Region, Tanzania

281 c. Kilbourne Hole, New Mexico

282 Figure 4 –Structural change associated with the OEN→HPCEN2 phase transition. O3-O3-O3 angle is

283 marked as θ in the figure. The largest change of θ occurs on the A site tetrahedral which is shown on the

284 top right.

285

Table 1: Comparison of Raman frequencies from previous studies

OEN, ambient condition							HPCEN2, normalized to 12.5GPa				
Stalder et al.	Huang et al.	Lin	Chopelas	This study			Lin	Chopelas	This study		
2009	2000	2003	1999	ZABG	TAN	KBH	2003	1999	ZABG	TAN	KBH
		83	83				94.7	94.9			
		106.8					135.9	139.1			
		115.4	115				166	*168.8*	**168.3**		
133.8		**134.3**	134	**137.4**			174.6	178.1	*179.7*		
		155.3	153		155.7	*151.4*	183				
		161.5				160	196.4	197.5	**199.2**	195.7	
		166.7	166	**170.2**	169.3	169.7	204				
				190.1	190.9		224.4	225.5	**227.9**	**223.7**	223.8
197.5		196.9	197	196.5	**197.1**	**193.7**	231.8				
				201.1			250.5	251.7	**254.4**	**251.7**	**251.3**
206.4		*206.5*		**208.3**			262.1		267.5		
			237	**240.1**			272	273.9	276.2		*269*
239	**238**	**238.2**	239	**241.1**	**238.2**	**238.4**			280.8		
		244.8	245	246.3	248.9		290.2	291.6	295.3	*288.7*	*289.7*
			261	**260.8**	*257.9*		304.1				*298.3*
				271.6			320.3	*314.5*	**323.6**	**318.9**	320
		278.2			**276.6**				**329.4**		
				286.5		284	337.2	338	**341.3**	**338.4**	335.7
302.5	**298**	301.5	302	**303.2**	300.7	*300.5*			*345.6*		
		323.3				320.1			*358.1*		
		327.7			**328.9**		373.4		*377.7*	**368.5**	
				340.3			381.5	*383.4*	*388.7*	**377.6**	*382.9*
				342.9			393.6	395.1	**399.6**	**395.3**	**394.5**
343.9	**344**	**343.5**	343	**345.4**	**339.9**	**345.3**	406.3	407	**412.1**	**404.4**	*404.7*

				374		
385.2		383.8		**381**	**381.7**	*387*
402.8	407	402.1	402	**402.6**	**399**	**407.6**
422.7	422	421.7	422	424.2	418.5	
445.9	447	445.5	446	*445.4*	443.2	444.3
				448		
		458.8	457	458.6	*459.9*	
		472.9		*478.7*	*476.4*	
			487	*488.3*		
527	522	524.9	519	**528.1**	**521**	**523.5**
					533.7	
540.8	543		540	541.9	544.7	*538*
553.5	551	551.5	553	554.5		**550.2**
581	582	580.3	580	**582.1**	**578.5**	574.9
		594.5			*593.9*	
664.8	**665**	**663.8**	665	**664.9**	***662.1***	**661.8**
687.1	**685**	**686.1**	687	**687.7**	***684.2***	**684.2**
						736.1
	751	750.7		752.7	*753.3*	**753.9**
853.2	856	851.1		**851**	**852.9**	848.7
			886			
927.9	**931**	926.6	927	929.6	929.7	929.3
936.5		935.2	937		938.6	*940.9*
1013.2	**1013**	**1011.3**	1014			
1034.7	**1035**	**1032.9**	1034			

Note: **strong** peaks are in **bold** font;
weak peaks are in *inclined grey* font;
Intermediate peaks are in normal font.

428.9	431.2	430.2	427.8	
	434.9	**436.3**		
445.8	447.3	**452.9**	**444.4**	**443.6**
462.7	466.3	**469.3**	*463.7*	
476.1	476.5	**480.2**	**475.6**	**475.3**
493.8	496.8	**499.4**	*493.9*	488.5
511.7			*507.6*	
533.6		528.9	*525.4*	
557.5	559.8	**562.9**	**557.1**	**557.8**
565.6		**570.9**	*569.8*	
587.8	*578.7*	583.3		*581*
		600.9		*598.5*
		607.2		
		620.4	616.1	*616*
704.1	704.1	708.4	706.9	701.3
716.5	**716.2**	**719.6**	**716.5**	**716**
725.3				
735.2	**736.1**	**739.8**	**735.9**	**735.3**
		780.1		
		814		
847	851.9	**856.1**		855.8
873.5		864.5	*861.7*	*865.4*
887.6	888.9	**893.1**	893.8	*893.2*
924.1	924.7			
963.6	955.3	969.5	*969.4*	*970*
1030.2				
1056.5	**1055.5**			
1075	**1073.3**			
1092.8	**1093.3**			

Table 2. Pressure dependence of the Raman frequencies for all three samples

OEN $v = v_0 + a \times P + b \times P \times 10^2$												HPCEN $v = v_0 + a \times P$								
ZABG near pure $MgSiO_3$				TAN Fe-bearing Al-free OEN				KBH Fe,Al-bearing OEN				ZABG near pure $MgSiO_3$			TAN Fe-bearing Al-free			KBH Fe,Al-bearing		
v_0	a	b	R^2	v_0	a	b	R^2	v_0	a	b	R^2	v_0	a	R^2	v_0	a	R^2	v_0	a	R^2
137.4(10)	**5.2(5)**	**-38.8(41)**	**0.954**	155.7(5)	0.8(2)	4.0(12)	0.989	*151.4(10)*	*1.3(3)*	*-0.3(17)*	*0.969*	**157.8(7)**	**0.8(1)**	**0.926**	181.5(15)	1.1(1)	0.818	202.6(22)	1.7(2)	0.919
170.2(3)	**2.1(1)**	**-5.4(7)**	**0.993**	169.3(6)	1.6(2)	-1.6	0.985	160.0(9)	0.3(2)	3.5(11)	0.925	*169.4(7)*	*0.8(1)*	*0.919*	**211.0(7)**	**1.0(1)**	**0.938**	**235.0(11)**	**1.3(1)**	**0.963**
190.1(9)	2.1(2)	-6.0(11)	0.981	**197.1(5)**	**0.4(2)**	**0.9(11)**	**0.909**	169.7(5)	2.0(1)	-5.3(5)	0.98	**191.6(7)**	**0.6(1)**	**0.828**	**237.9(8)**	**1.1(1)**	**0.932**	*248.4(45)*	*1.6(3)*	*0.805*
196.5(10)	1.6(3)	-4.0(16)	0.951	190.9(36)	6.0(8)	-21.2(42)	0.972	**193.7(7)**	**1.4(2)**	**-1.9(9)**	**0.958**	**215.3(9)**	**1.0(1)**	**0.895**	*268.3(31)*	*1.6(2)*	*0.724*	*257.1(41)*	*2.6(3)*	*0.902*
201.1(19)	3.8(7)	-19.8(50)	0.847	**238.2(5)**	**1.7(2)**	**-3.7(11)**	**0.986**	**238.4(4)**	**1.7(1)**	**-3.8(5)**	**0.986**	**241.8(7)**	**1.0(1)**	**0.945**	**300.4(10)**	**1.5(1)**	**0.938**	*191.2(219)*	*8.6(15)*	*0.938*
208.3(9)	**3.0(2)**	**-4.5(14)**	**0.992**	248.9(13)	0.0(4)	10.2(28)	0.936	284.0(7)	2.0(1)	-2.9(7)	0.985	249.9(19)	1.4(1)	0.805	**315.4(16)**	**1.8(1)**	**0.905**	298.5(25)	1.7(2)	0.909
240.1(6)	**1.6(2)**	**-2.7(12)**	**0.976**	*257.9*	*3.4(2)*	*-3.6(17)*	*0.997*	*300.5(34)*	*1.0(8)*	*8.0(50)*	*0.869*	256.7(13)	1.6(1)	0.915	**338.1(20)**	**2.4(1)**	**0.923**	309.5(24)	2.1(2)	0.936
241.1(8)	**2.9(2)**	**-7.3(15)**	**0.989**	**276.6(9)**	**3.5(2)**	**-10.4(14)**	**0.984**	320.1(9)	4.5(2)	-5.7(10)	0.993	255.5(19)	2.0(1)	0.902	**343.9(16)**	**2.7(1)**	**0.951**	*360.8(66)*	*1.8(5)*	*0.725*
246.3(10)	3.9(3)	-10.1(17)	0.989	300.7(6)	2.0(2)	-2.7(15)	0.99	**345.3(6)**	**6.2(1)**	**-10.7(7)**	**0.998**	273.4(17)	1.8(1)	0.891	**371.2(11)**	**1.9(1)**	**0.957**	**370.6(13)**	**1.9(1)**	**0.977**
260.8(7)	**3.9(2)**	**-6.7(13)**	**0.995**	**328.9(11)**	**2.8(3)**	**2.5(18)**	**0.994**	*387.0(68)*	*1.4(33)*	*14.4(226)*	*0.922*	**305.3(10)**	**1.5(1)**	**0.935**	**364.8(17)**	**3.2(1)**	**0.96**	*365.9(98)*	*3.1(6)*	*0.849*
271.6(61)	**5.3(13)**	**-19.2(67)**	**0.853**	**339.9(12)**	**6.8(4)**	**-12.6(27)**	**0.995**	**407.6(6)**	**3.9(1)**	**-7.8(6)**	**0.995**	**310.2(16)**	**1.5(1)**	**0.876**	396.6(26)	2.5(2)	0.868	**397.7(50)**	**3.7(3)**	**0.913**
286.5(7)	**2.8(2)**	**-5.5(11)**	**0.993**	**381.7(8)**	**3.7(3)**	**-3.0(19)**	**0.994**	444.3(11)	2.5(2)	-0.4(13)	0.976	**319.8(13)**	**1.7(1)**	**0.93**	**398.6(29)**	**3.7(2)**	**0.923**	**450.7(11)**	**2.0(1)**	**0.983**
303.2(5)	**2.6(1)**	**-4.6(9)**	**0.994**	**399.0(10)**	**5.4(3)**	**-14.4(24)**	**0.992**	**523.5(7)**	**2.7(2)**	**-0.4(9)**	**0.991**	*312.8(56)*	*2.6(4)*	*0.788*	433.4(23)	2.4(2)	0.948	438.7(52)	4.0(4)	0.933
342.9(119)	*3.6(21)*	*-7.2(93)*	*0.947*	418.5(18)	2.3(7)	3.5(53)	0.972	*538.0(9)*	*1.1(5)*	*8.7(29)*	*0.999*	*339.8(35)*	*1.5(2)*	*0.793*	**451.9(11)**	**1.9(1)**	**0.958**	**516.1(23)**	**3.3(2)**	**0.977**
340.3(81)	*6.4(15)*	*-23.6(69)*	*0.893*	443.2(7)	2.8(2)	-3.5(18)	0.991	**550.2(8)**	**2.7(2)**	**-0.7(10)**	**0.989**	*342.6(22)*	*2.8(2)*	*0.957*	*457.6(18)*	*2.9(1)*	*0.956*	*551.7(37)*	*2.3(2)*	*0.949*
345.4(11)	**6.9(3)**	**-12.2(22)**	**0.996**	*459.9(16)*	*2.0(7)*	*1.1(52)*	*0.961*	574.9(11)	2.5(2)	-2.8(14)	0.971	*351.6(30)*	*3.0(2)*	*0.936*	*473.8(42)*	*2.7(3)*	*0.913*	*571.1(45)*	*2.2(3)*	*0.855*
374.0(24)	*6.1(6)*	*-13.7(39)*	*0.979*	*476.4(14)*	*5.5(4)*	*-11.4(26)*	*0.988*	**661.8(4)**	**3.8(1)**	**-3.3(6)**	**0.998**	**371.9(19)**	**2.2(1)**	**0.905**	*478.5(43)*	*3.8(3)*	*0.927*	*598.5(27)*	*1.4(2)*	*0.847*
381.0(32)	**6.2(10)**	**-13.1(64)**	**0.947**	**521.0(6)**	3.1(2)	-1.0(14)	0.996	**684.2(5)**	**3.9(1)**	**-5.5(6)**	**0.997**	**374.3(36)**	**3.0(3)**	**0.856**	**524.3(22)**	**2.6(2)**	**0.916**	658.1(57)	3.5(4)	0.926
402.6(9)	**5.3(3)**	**-12.8(17)**	**0.994**	*533.7(28)*	*2.2(10)*	*4.5(71)*	*0.925*	*736.1(42)*	*3.4(13)*	*-12.2(72)*	*0.802*	401.2(17)	2.3(1)	0.929	*545.8(47)*	*1.9(3)*	*0.625*	**674.1(26)**	**3.3(2)**	**0.969**
424.2(43)	2.9(15)	-1.7(106)	0.8	544.7(20)	4.0(6)	-6.8(42)	0.962	**753.9(13)**	**2.6(3)**	**3.4(16)**	**0.985**	**407.6(27)**	**2.3(2)**	**0.843**	592.1(17)	1.9(1)	0.908	**690.6(22)**	**3.6(1)**	**0.981**
445.4(68)	1.1(14)	8.0(68)	0.978	**578.5(4)**	2.0(1)	-0.8(9)	0.995	848.7(9)	1.9(2)	5.7(11)	0.99	**423.9(46)**	**2.3(3)**	**0.644**	679.0(25)	2.2(2)	0.875	810.2(47)	3.7(3)	0.922
448.0(9)	2.4(3)	0.4(19)	0.986	*593.9(9)*	*3.5(4)*	*-8.4(29)*	*0.991*	929.3(8)	4.0(2)	-4.3(10)	0.993	**441.7(20)**	**2.2(1)**	**0.903**	**680.6(15)**	**2.9(1)**	**0.964**	*841.1(23)*	*1.9(2)*	*0.982*
458.6(17)	3.1(5)	-1.0(34)	0.965	***662.1(9)***	**4.0(3)**	**-3.3(21)**	**0.994**	*940.9(38)*	*5.7(10)*	*-6.3(64)*	*0.974*	**456.8(15)**	**1.9(1)**	**0.916**	**697.8(16)**	**3.1(1)**	**0.962**	*844.7(24)*	*3.9(2)*	*0.988*
478.7(22)	*2.3(5)*	*1.8(29)*	*0.983*	***684.2(5)***	**3.8(2)**	**-4.1(12)**	**0.997**					**463.9(22)**	**2.8(2)**	**0.923**	*840.8(29)*	*1.7(2)*	*0.706*	*947.7(21)*	*1.8(1)*	*0.935*
488.3(12)	*3.4(4)*	*1.3(24)*	*0.99*	*753.3(20)*	*2.6(8)*	*4.8(72)*	*0.967*					489.7(35)	3.1(3)	0.869	850.4(54)	3.5(4)	0.911			

528.1(11)	**2.1(3)**	**3.5(23)**	**0.982**	**852.9(16)**	**1.1(5)**	**9.1(37)**	**0.963**
541.9(5)	1.1(2)	10.1(13)	0.997	929.7(19)	3.5(5)	-0.2(29)	0.993
554.5(18)	2.3(5)	2.9(36)	0.96	938.6(22)	5.7(5)	-5.8(32)	0.995
582.1(6)	**2.0(2)**	**-0.3(11)**	**0.992**				
664.9(8)	**4.0(3)**	**-3.8(17)**	**0.994**				
687.7(7)	**4.0(2)**	**-5.6(13)**	**0.996**				
752.7(12)	3.2(4)	1.7(25)	0.989				
851.0(11)	**1.2(3)**	**8.4(22)**	**0.979**				
929.6(8)	3.7(2)	-2.1(15)	0.995				

Note: **strong** peaks are in **bold** format;

weak peaks are in *inclined grey* format;

Intermediate peaks are in normal format.

528.5(28)	**2.8(2)**	**0.878**		*937.0(47)*	*2.6(3)*	*0.844*	
534.4(23)	**2.9(2)**	**0.92**					
550(23)	2.7(2)	0.912					
582.5(33)	*1.5(2)*	*0.791*					
574.6(36)	*2.6(3)*	*0.896*					
595.1(18)	**2.0(1)**	**0.901**					
673.4(23)	2.8(2)	0.913					
685.3(15)	**2.7(1)**	**0.963**					
701.9(17)	**3.0(1)**	**0.957**					
738.8(24)	*3.3(2)*	*0.962*					
782.9(36)	*2.5(3)*	*0.86*					
824.9(13)	**2.5(1)**	**0.963**					
846.4(23)	1.4(2)	0.764					
853.8(22)	**3.1(2)**	**0.937**					
939.6(27)	2.4(2)	0.858					

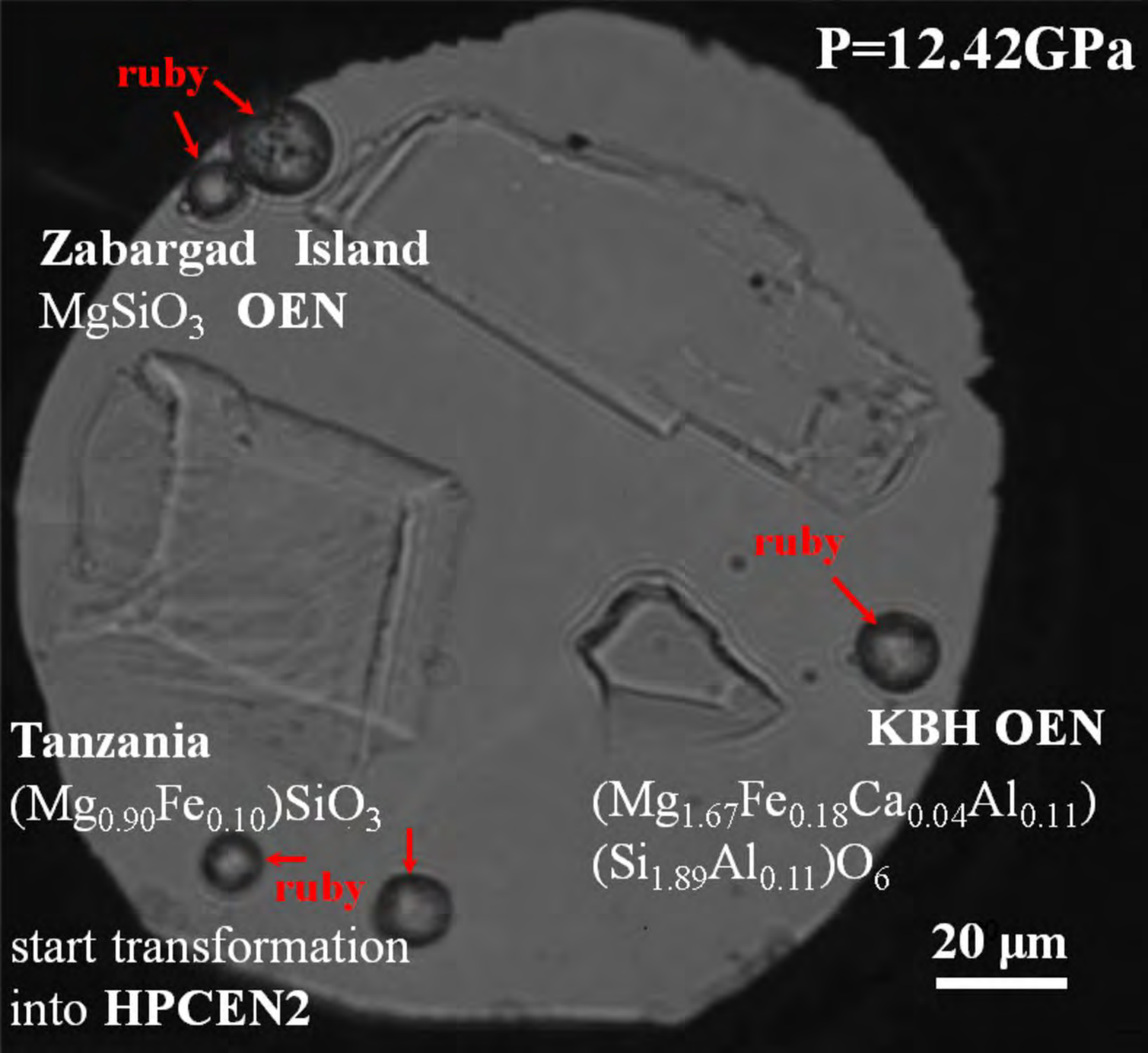
P=12.42GPa
ruby
Zabargad Island
$MgSiO_3$ OEN
ruby
KBH OEN
$(Mg_{1.67}Fe_{0.18}Ca_{0.04}Al_{0.11})(Si_{1.89}Al_{0.11})O_6$
Tanzania
$(Mg_{0.90}Fe_{0.10})SiO_3$
ruby
start transformation into HPCEN2
20 μm

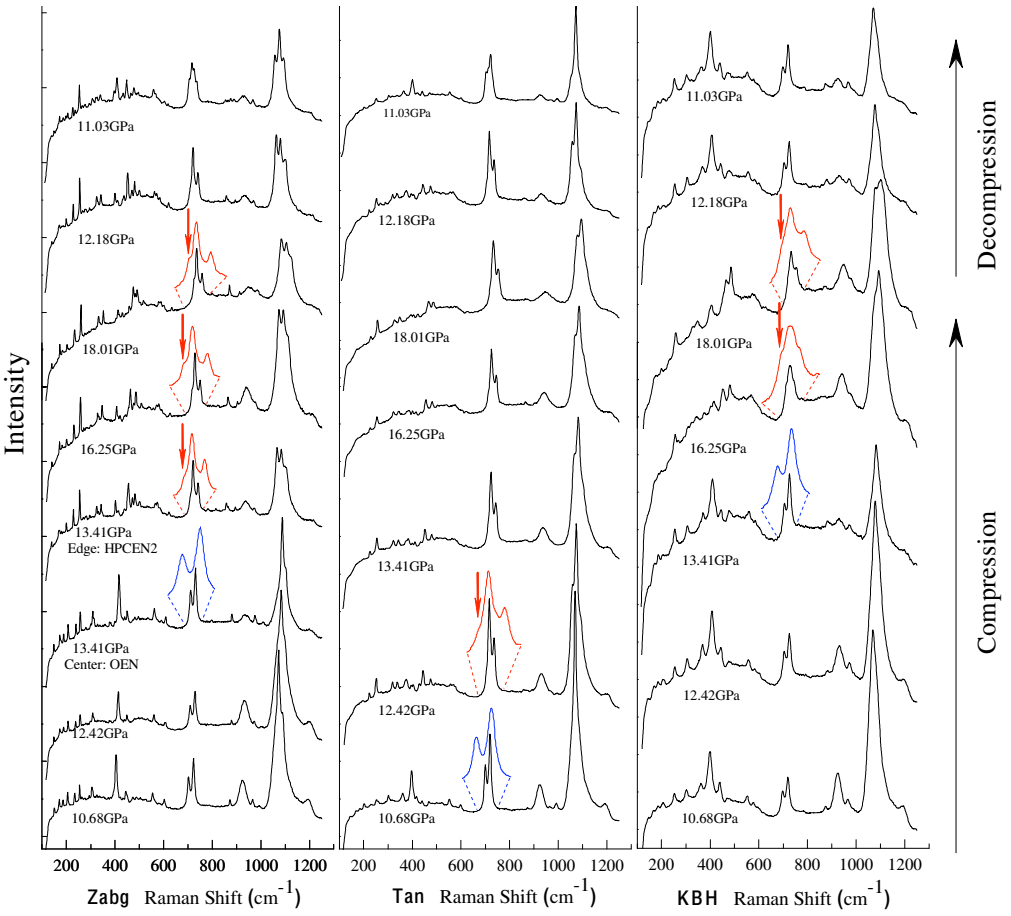
Intensity
11.03GPa
12.18GPa
18.01GPa
16.25GPa
13.41GPa
Edge: HPCEN2
13.41GPa
Center: OEN
12.42GPa
10.68GPa
11.03GPa
12.18GPa
18.01GPa
16.25GPa
13.41GPa
12.42GPa
10.68GPa
11.03GPa
12.18GPa
18.01GPa
16.25GPa
13.41GPa
12.42GPa
10.68GPa
Decompression
Compression
200 400 600 800 1000 1200
200 400 600 800 1000 1200
200 400 600 800 1000 1200
Zabg Raman Shift (cm-1)
Tan Raman Shift (cm-1)
KBH Raman Shift (cm-1)

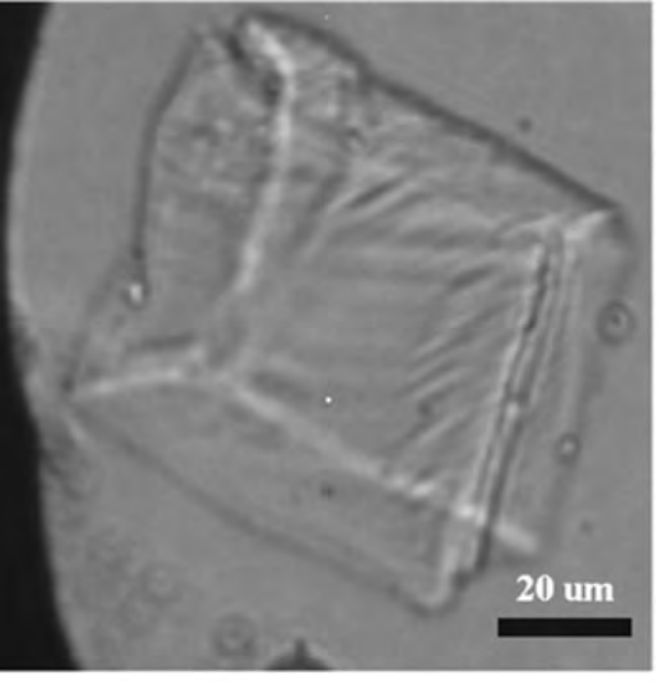

13.13 GPa

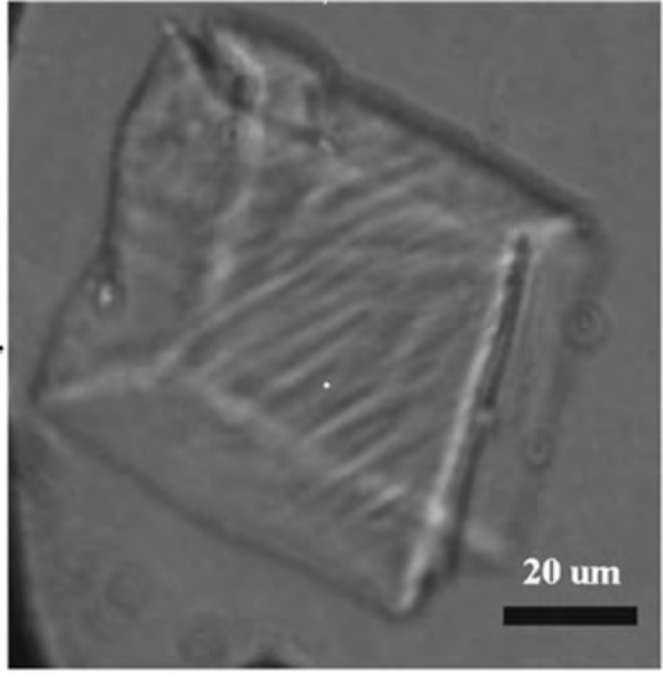

13.41GPa

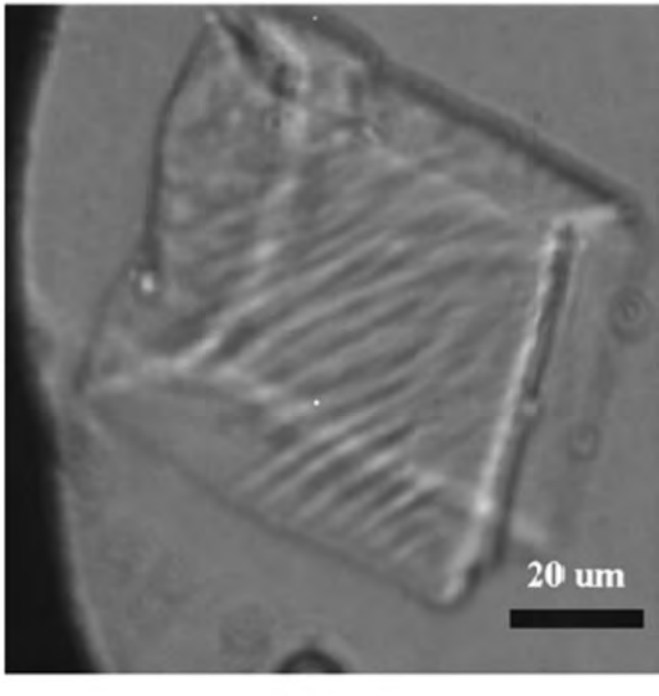

13.87GPa

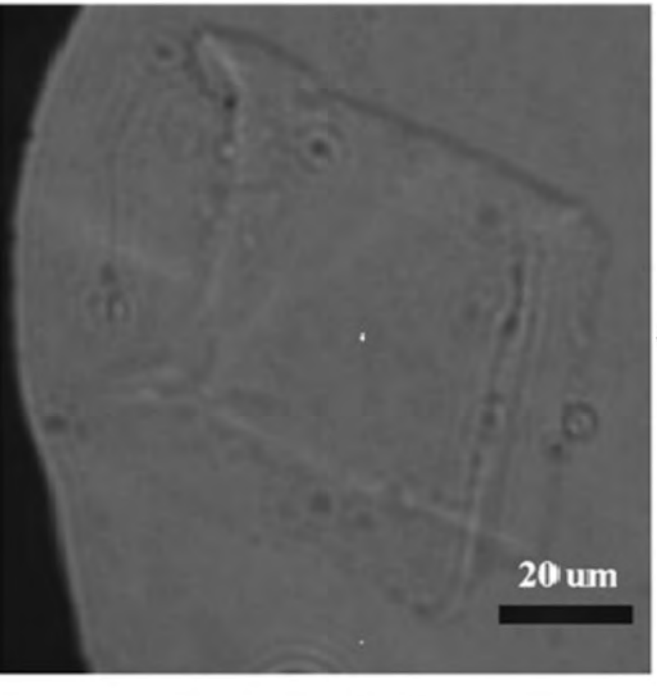

14.66GPa

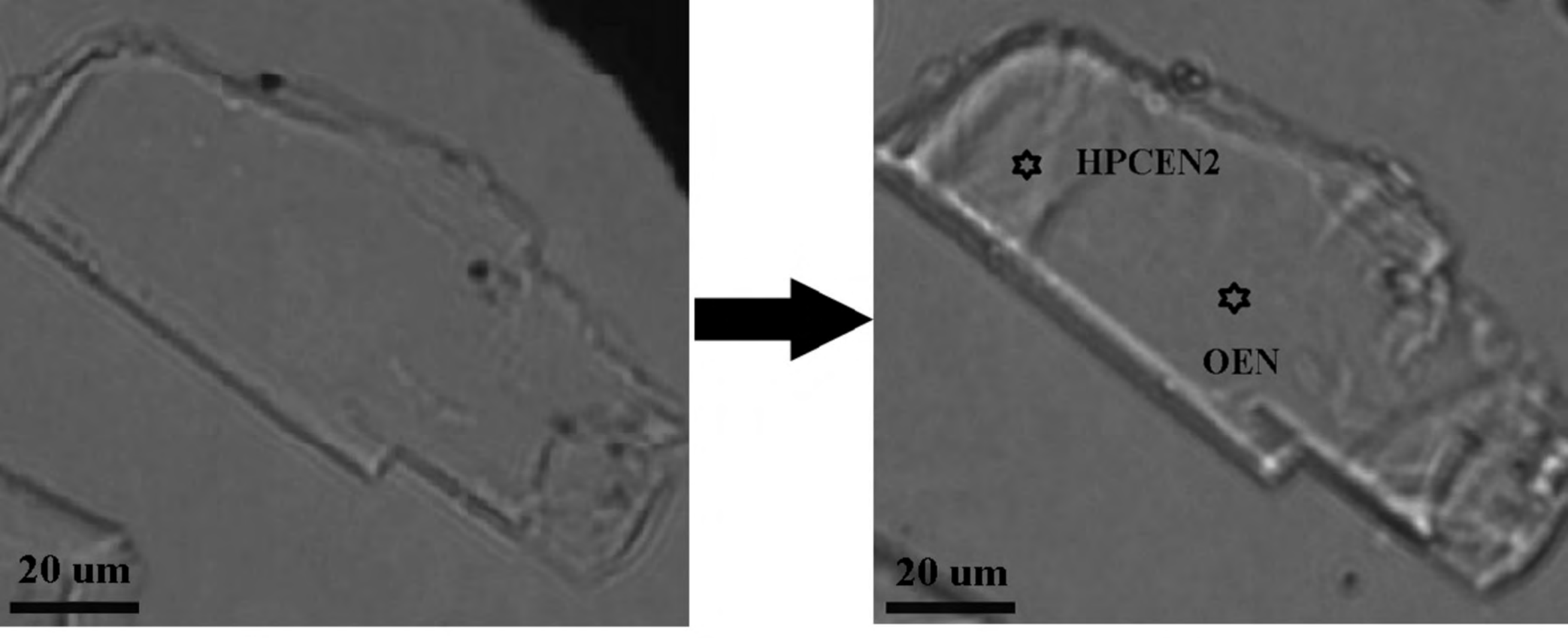

12.42GPa

13.87GPa

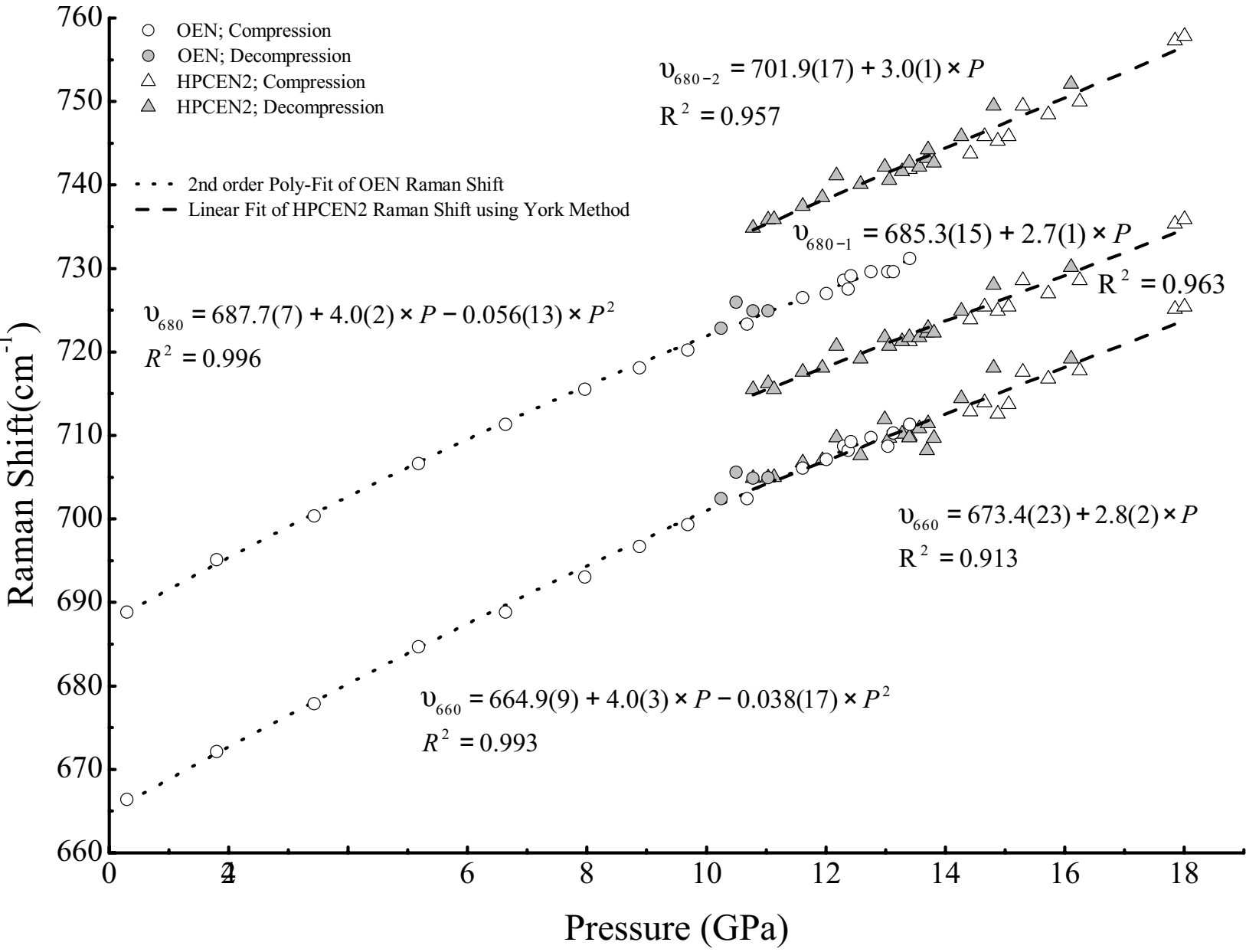
OEN; Compression
OEN; Decompression
HPCEN2; Compression
HPCEN2; Decompression
2nd order Poly-Fit of OEN Raman Shift
Linear Fit of HPCEN2 Raman Shift using York Method
υ680-2 = 701.9(17) + 3.0(1) × P
R2 = 0.957
υ680-1 = 685.3(15) + 2.7(1) × P
R2 = 0.963
υ680 = 687.7(7) + 4.0(2) × P − 0.056(13) × P2
R2 = 0.996
υ660 = 673.4(23) + 2.8(2) × P
R2 = 0.913
υ660 = 664.9(9) + 4.0(3) × P − 0.038(17) × P2
R2 = 0.993
Raman Shift(cm-1)
Pressure (GPa)
760
750
740
730
720
710
700
690
680
670
660
0
2
4
6
8
10
12
14
16
18

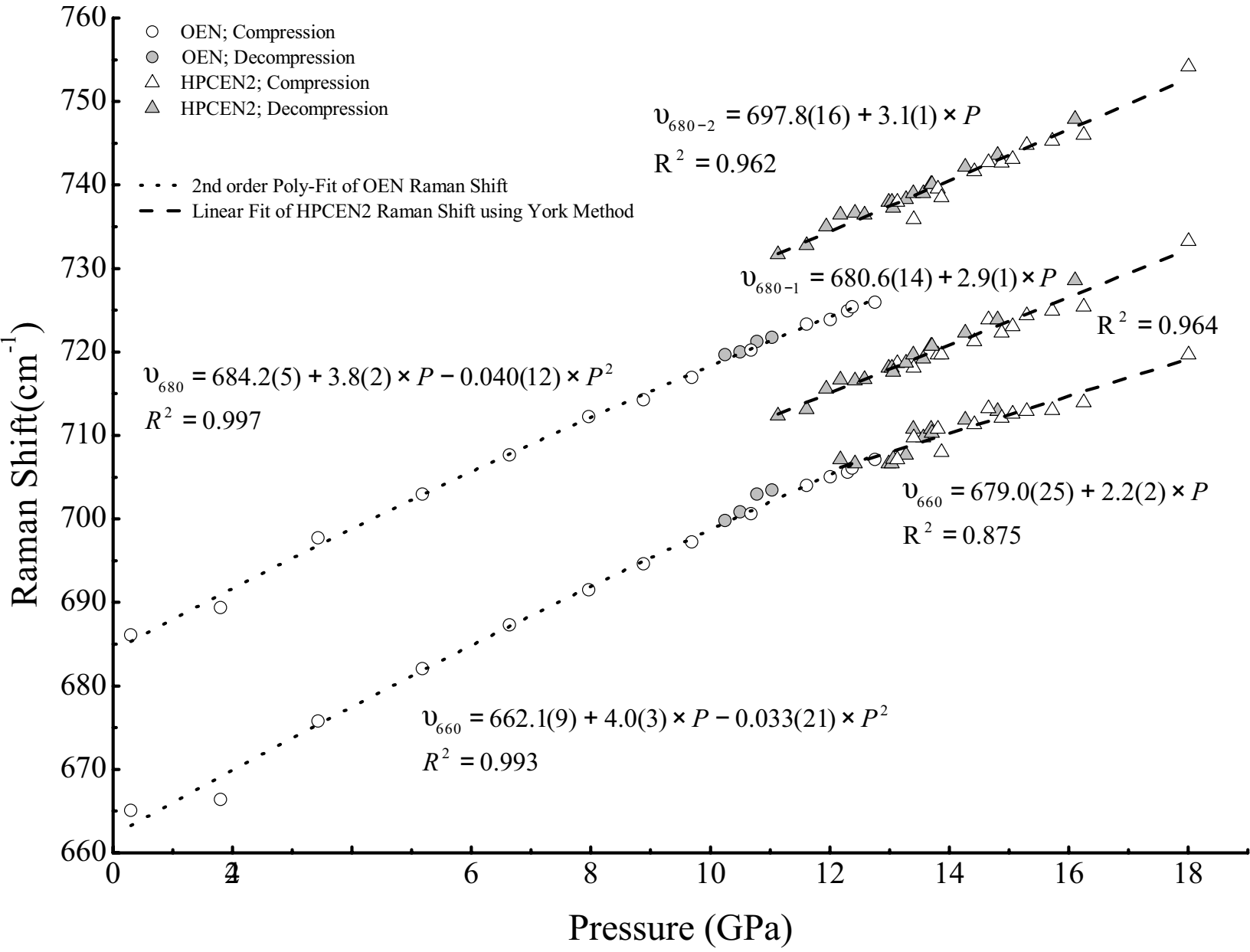
OEN; Compression
OEN; Decompression
HPCEN2; Compression
HPCEN2; Decompression
2nd order Poly-Fit of OEN Raman Shift
Linear Fit of HPCEN2 Raman Shift using York Method
υ680-2 = 697.8(16) + 3.1(1) × P
R 2 = 0.962
υ680-1 = 680.6(14) + 2.9(1) × P
R 2 = 0.964
υ680 = 684.2(5) + 3.8(2) × P − 0.040(12) × P2
R2 = 0.997
υ660 = 679.0(25) + 2.2(2) × P
R 2 = 0.875
υ660 = 662.1(9) + 4.0(3) × P − 0.033(21) × P2
R2 = 0.993
Raman Shift(cm-1)
Pressure (GPa)
760
750
740
730
720
710
700
690
680
670
660
0
2
4
6
8
10
12
14
16
18

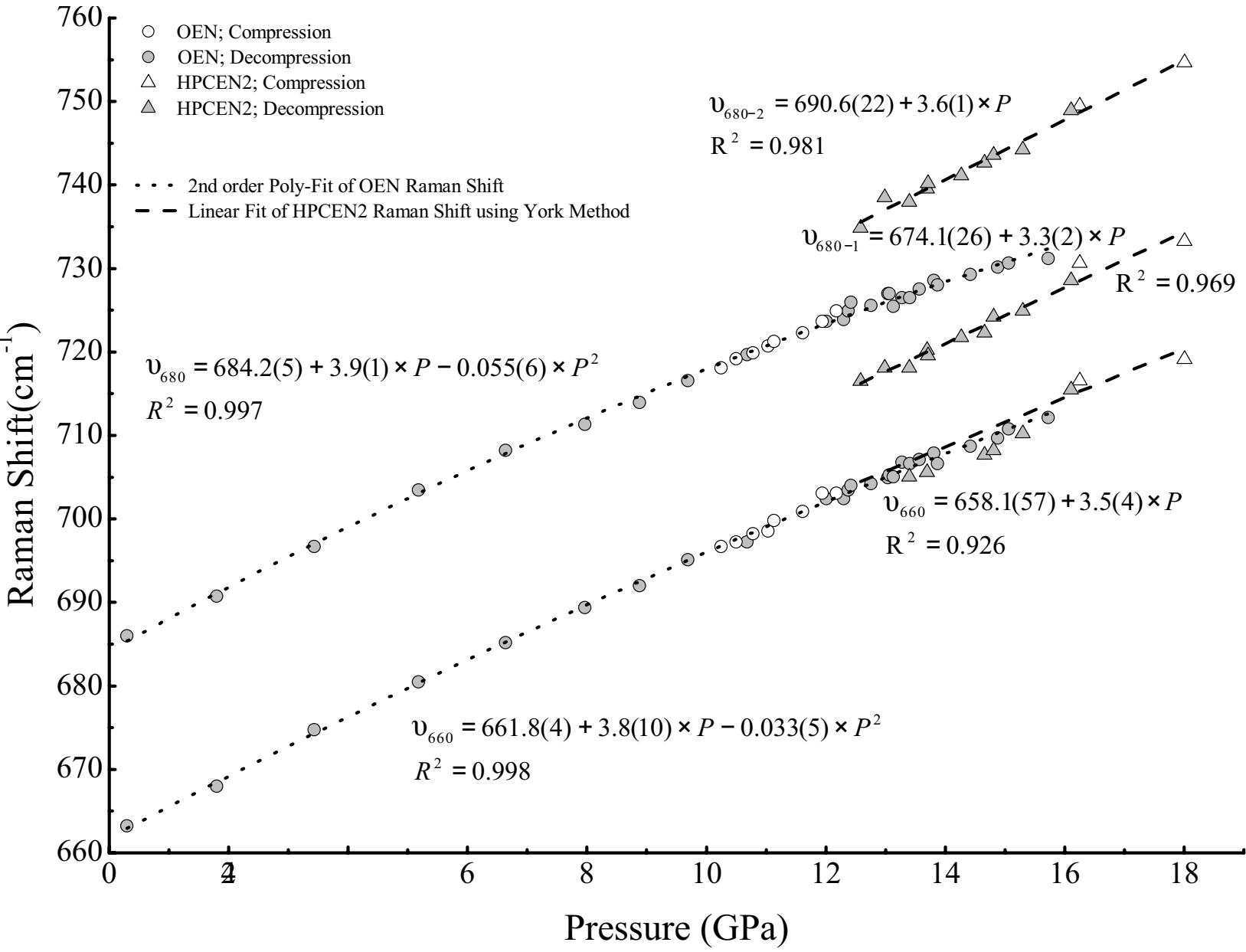
OEN; Compression
OEN; Decompression
HPCEN2; Compression
HPCEN2; Decompression
2nd order Poly-Fit of OEN Raman Shift
Linear Fit of HPCEN2 Raman Shift using York Method
$\upsilon_{680-2} = 690.6(22) + 3.6(1) \times P$
$R^2 = 0.981$
$\upsilon_{680-1} = 674.1(26) + 3.3(2) \times P$
$R^2 = 0.969$
$\upsilon_{680} = 684.2(5) + 3.9(1) \times P - 0.055(6) \times P^2$
$R^2 = 0.997$
$\upsilon_{660} = 658.1(57) + 3.5(4) \times P$
$R^2 = 0.926$
$\upsilon_{660} = 661.8(4) + 3.8(10) \times P - 0.033(5) \times P^2$
$R^2 = 0.998$
Raman Shift(cm^{-1})
Pressure (GPa)
760
750
740
730
720
710
700
690
680
670
660
0
2
4
6
8
10
12
14
16
18

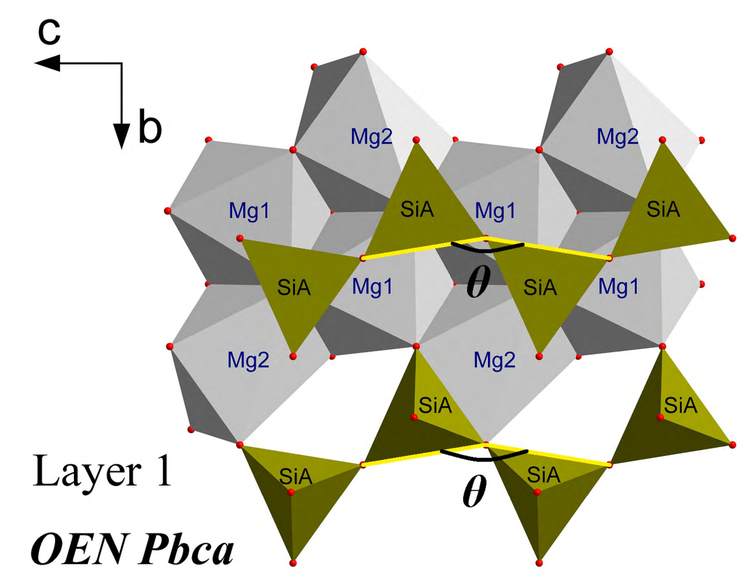
c
b
Mg2
Mg1
SiA
θ
Layer 1
OEN Pbca

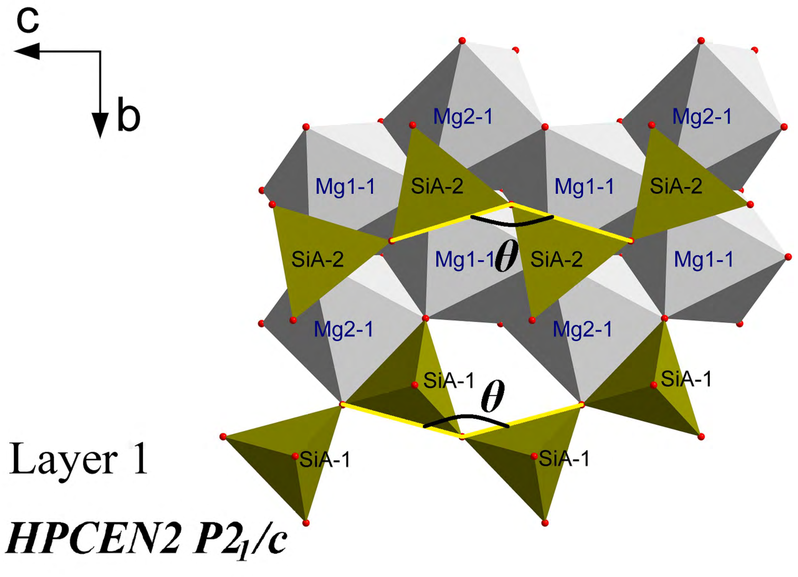
c
b
Mg2-1
Mg1-1
SiA-2
SiA-1
θ
Layer 1
HPCEN2 P2₁/c

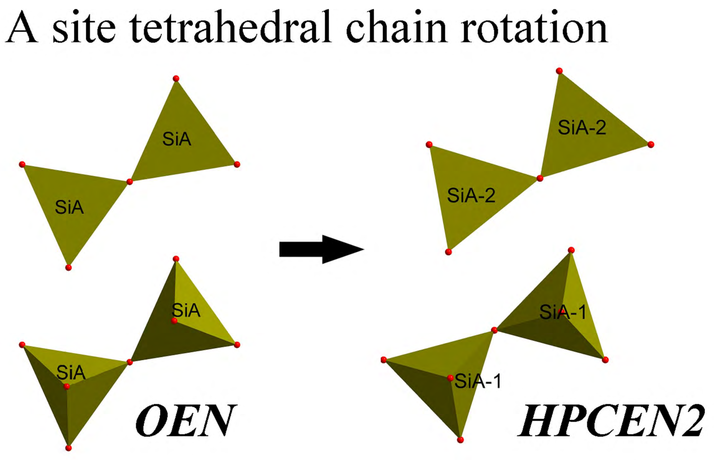
A site tetrahedral chain rotation
SiA
SiA-2
SiA-1
OEN
HPCEN2

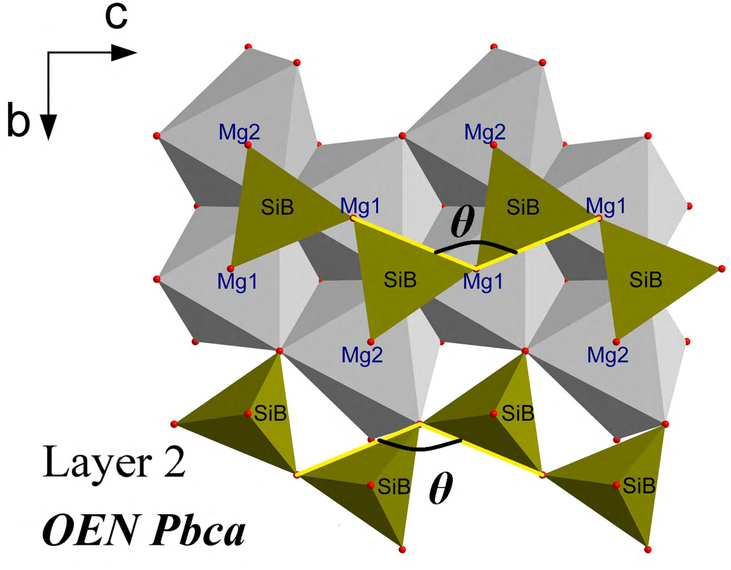
c
b
Mg2
Mg1
SiB
θ
Layer 2
OEN Pbca

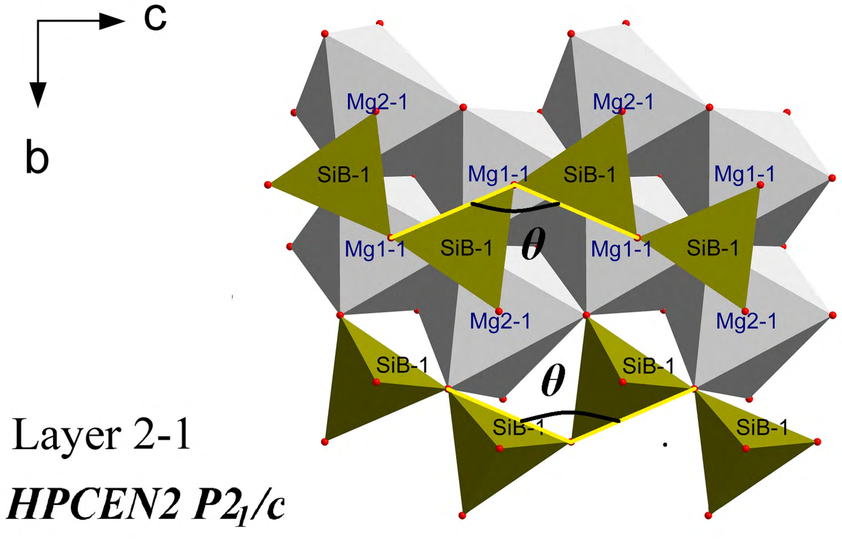
c
b
Mg2-1
Mg1-1
SiB-1
θ
Layer 2-1
HPCEN2 P2₁/c

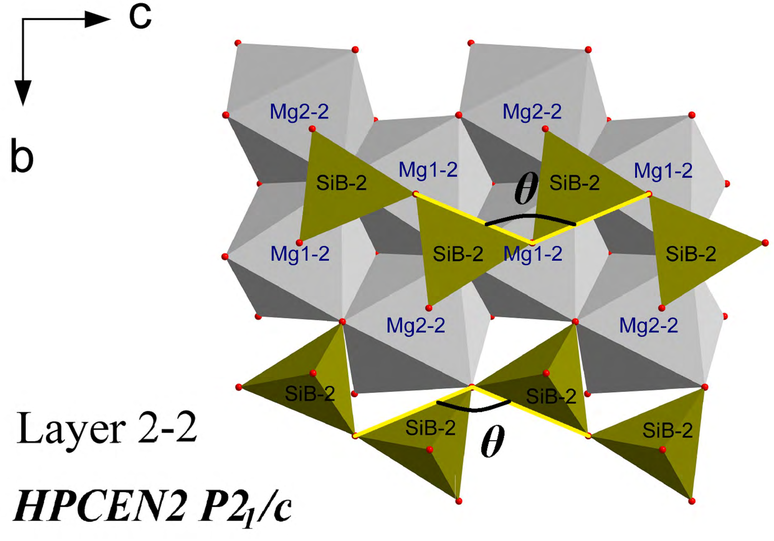
c
b
Mg2-2
Mg1-2
SiB-2
θ
Layer 2-2
HPCEN2 P2₁/c